ADVANCED BIOSYSTEMS
www.adv-biosys.com

Check for updates

Early Committed Clockwise Cell Chirality Upregulates Adipogenic Differentiation of Mesenchymal Stem Cells

*Yuanye Bao, Siying Wu, Lok Ting Chu, Hoi Kwan Kwong, Hogi Hartanto, Yaozhun Huang, Miu Ling Lam, Raymond H. W. Lam, and Ting-Hsuan Chen**

Cell chirality is observed with diverse forms and coordinates various left-right (LR) asymmetry in tissue morphogenesis. To give rise to such diversity, cell chirality may be coupled with cell differentiation. Here, using micropatterned human mesenchymal stem cells (hMSCs), an early committed clockwise (CW) cell chirality that can itself upregulate the adipogenic differentiation is reported. hMSC chirality enables a positively tilted chiral orientation on micropatterned stripes. When cultured as single cells on circular micropatterns, an anticlockwise (ACW)-biased nucleus rotation and swirling pattern of actin filament are observed. Interestingly, with adipogenic induction for 3–6 days, such chirality is reversed to negative chiral orientation and CW-biased rotation, which is earlier than the maturation of other differentiation markers, and consistently expressed in terminally differentiated adipocytes. Using latrunculin A (LatA), cytochalasin D (CD), and nocodazole (Noco) that forces a CW-biased actin filament and nucleus rotation resembling the early differentiated chirality upon adipogenic induction, an upregulation of adipogenic differentiation is found. The result demonstrates that the early differentiated chirality may serve as a mechanical precursor to engage the lineage commitment, suggesting a feedback mechanism of chiral actin in regulating cell differentiation and LR morphogenesis.

1. Introduction

Cell chirality is an intrinsic, left-right (LR)-biased cell mechanics driven by intracellular molecular handedness.[1–4] Examples were found such as active torsion of cells[1,5,6] and chiral skew event that establishes an uneven distribution of cells in *Caenorhabditis elegans* embryos.[7] It is believed that cell chirality can ultimately determine the LR asymmetry in morphogenesis.[2] For example, chirality has been found in *Xenopus* egg cortex before fertilization,[1] and can be passed down to more differentiated cells that establish LR body axis of animal body plan,[7] organ distribution,[8–10] and epithelial movement that leads to axial torsion and overall handedness of hindgut.[11,12] For specialized adult cells derived from somatic tissue, footprints of cell chirality can still be seen by their ability of generating cellular torque,[6,13] migration with LR bias,[14–16] or forming specific alignment in the multicellular level.[15,17,18] Through cell–cell communication, the chiral behavior causes LR-biased cell assembly of multicellular structure[15] and regulates permeability of intercellular junctions.[19] Clearly, cell chirality can be manifested in diverse forms and coordinate different morphogenic dynamics, resulting in distinct forms of tissue and organ architecture.

Actin cytoskeleton plays an important role in cell chirality. When cultured on micropatterned substrate, the accumulation of actomyosin stress fibers at micropattern boundary is essential to activate the LR bias in cell migration and orientation.[15,17] Molecular studies suggest helical motion of actin filament as the underlying mechanism for the chirality at cellular level.[20,21] Functioning as a built-in machinery, actomyosin cytoskeleton allows chiral nucleus rotation of single cell[21] and generation of cellular torque with rotational bias.[13] Through a series of amplification process, the actin chirality ultimately determines the symmetry breaking in early embryonic development,[1,7,22] cardiac looping,[4,8,23] and organ laterality[9] in vivo.

To give rise to such diverse forms of cell chirality, cell differentiation should play a role.[13,15,17] Cell differentiation is a process coupling with chemical[24] and physical factors.[25–27] Based on variation of key proteins in cytoskeleton,[28] cytoskeleton can be changed at early stage of cell differentiation, as shown by upregulation of cytoskeletal contractility[29] and cell morphological features, which can even forecast the cell lineage fate.[28] It suggests that cytoskeletal components, particularly actin, may early respond to the induction of cell differentiation and then actively participate the signal cascades to engage cell fate. Evidences can be found by regulation of cell differentiation via changed cell shape and cell spreading by physical cues[30–38]

Dr. Y. Y. Bao, S. Y. Wu, L. T. Chu, H. K. Kwong, H. Hartanto, Dr. Y. Z. Huang, Prof. R. H. W. Lam, Prof. T.-H. Chen
Department of Biomedical Engineering
City University of Hong Kong
Kowloon, Hong Kong Special Administrative Region
E-mail: thchen@cityu.edu.hk
Prof. M. L. Lam
School of Creative Media
City University of Hong Kong
Kowloon, Hong Kong Special Administrative Region
The ORCID identification number(s) for the author(s) of this article can be found under https://doi.org/10.1002/adbi.202000161.

DOI: 10.1002/adbi.202000161

 © 2020 Wiley-VCH GmbH

and inhibition of actin polymerization by chemical cues.[39–41] Through this feedback mechanism, cytoskeletal components, particularly actin, serve as key mediators to early respond to the induction of cell differentiation and further amplify the signal cascades. Thus, since cell chirality is also governed by actin cytoskeleton, it may also early correspond to lineage specification,[42] allowing the specification and commitment of LR asymmetry in early stage of morphogenesis. However, it remains largely unknown.

Using micropatterning on human mesenchymal stem cells (hMSCs), here we report an early differentiated CW chirality that can regulate the commitment of adipogenic lineage. Assessed based on cell orientation and nucleus rotation on cell-adherent micropatterns, hMSCs exhibit a positive cell orientation and anticlockwise (ACW)-biased nucleus rotation and swirling of actin filament. Importantly, with adipogenic induction for 3–6 days, the chiral orientation becomes negatively biased, and nucleus rotation and actin swirling becomes clockwise (CW)-biased. Such early modified cell chirality is consistent with that of cells at terminal differentiation and appears before the maturation of other standard differentiation markers. Furthermore, using latrunculin A (LatA), cytochalasin D (CD), and nocodazole (Noco) that forces a CW-biased actin filament and nucleus rotation resembling the early differentiated chirality upon adipogenic induction, adipogenic differentiation is upregulated. It suggests that chiral actin cytoskeleton differentiated at early stage of induction works as a mechanical precursor to substantiate the lineage commitment and guide the early pattern of tissue morphogenesis. This study demonstrates chiral actin as a key mediator in a closed feedback loop regulating cell differentiation, providing a new insight into stem cell research, mechanobiology, and LR morphogenesis.

2. Results

2.1. Chirality of hMSCs

We first studied the chirality of hMSCs via multicellular orientation. Undifferentiated hMSCs were seeded onto cell-adherent stripes with cell-adherent protein (FN) surrounded by cell-repellent molecules (Pluronic F127). Cells initially attached to the stripes and subsequently spread out, forming a specific chiral orientation (**Figure 1**A). We analyzed the cell orientation angle relative to the stripe boundary, which is defined positive when it is within 0° to 90° and negative when it is within −90° to 0° (Figure 1B). Four hours after seeding, some cells aligned with the stripe boundary, and no significant bias was observed between the percentage of cells with positive and negative orientation (Figure 1C). After 5 days, a significant positive appeared (64.1%, Figure 1C). Of note, the bias between positive and negative orientation was also statistically significant, suggesting the existence of cell chirality (Figure 1C).

We next tested whether the hMSC chirality exists in nucleus rotation of single cells.[13,21] Individual cells were seeded onto cell-adherent circular patterns surrounded by pluronic coating (Figure 1D). With reference to the long-axis of cell nucleus, the transient angular velocity of cell nucleus was recorded at each 10 min interval, and the percentages of transient CW and ACW rotation within the observation duration were compared to determine the rotational bias (Figure 1D). Our results showed that, on circular patterns with radius of 40 μm, nucleus rotation of undifferentiated hMSCs exhibited a significant ACW bias (52.7%), and such bias was more significant compared to that on other sizes of circular micropatterns (radius = 30 and 50 μm, Figure S1A,B, Supporting Information) or on other cell-adherent materials (laminin or plasma-treated petri dish, Figure S1C,D, Supporting Information). Moreover, on gear patterns, i.e., circular patterns notched with 12 radial insertion of cell-repellent bars (Figure S1E, Supporting Information), an even stronger ACW bias was shown (58.2%, Figure 1E). Together, the results demonstrated the existence of hMSC chirality by the ACW-biased nucleus rotation of single cells. Based on it, we chose the FN gear pattern with radius = 40 μm in the following measurement.

We next investigated the actin cytoskeleton associated with the chiral nucleus rotation of single cells. Previous findings revealed that, when cells are cultured on circular islands, their actin cytoskeleton forms a CW- or ACW-biased swirl pattern of dorsal stress fibers that are unidirectionally tilted with a tangential shift of transverse arc.[13,15,21,43] After the rotational assay on gear patterns mentioned above, the cells were fixed and stained (Figure 1F). Automated image processing was used to analyze the tilting angle of actin filament with respect to the radial axis of each cell. As such, the rotational bias of actin swirling pattern can be quantified (Figure 1F, see details in the Experimental Section). By collecting data from all cells, we found that the actin in undifferentiated hMSCs is ACW-biased, which is consistent with the ACW bias of nucleus rotation (Figure 1G), suggesting that the chiral swirling of actin cytoskeleton is involved.

2.2. Lineage Dependence of Cell Chirality

We next investigated the possible change of cell chirality during lineage specification. Three hours after plating the hMSCs on cell-adherent stripes, adipogenic and osteogenic induction medium (AM or OM) were applied. Interestingly, we observed a significant change of chiral orientation during cell differentiation on days 3 and 5. For cells with AM, cell morphology was less elongated (**Figure 2**A) as compared to cells with OM (Figure 2B). More importantly, cells with AM on day 3 orientated with a significant negative bias, which was very different from the positive orientation of cells in growth medium (GM) and with osteogenic induction (Figure 2C). On day 5, positive bias was observed in cell orientation of all three cases, while the same trend was observed, i.e., strongest bias in OM and weakest bias in adipogenic differentiation (Figure 2D). Of note, in such short duration of induction, Oil Red O staining was negative, and alkaline phosphatase (ALP) activity remains in low level (Figure S2A–C, Supporting Information). Also, quantitative PCR (qPCR) analysis of adipogenic markers, i.e., adiponectin[44] and PPARγ,[45] showed significantly lower expression than that of terminally differentiated adipocytes, and moderate lower expression of osteogenic marker, i.e., ALP,[46] than that of osteoblasts (Figure S2D, Supporting Information). Together, this result suggested that the chiral orientation is subject to change upon the lineage-specific induction. More strikingly, such

© 2020 Wiley-VCH GmbH

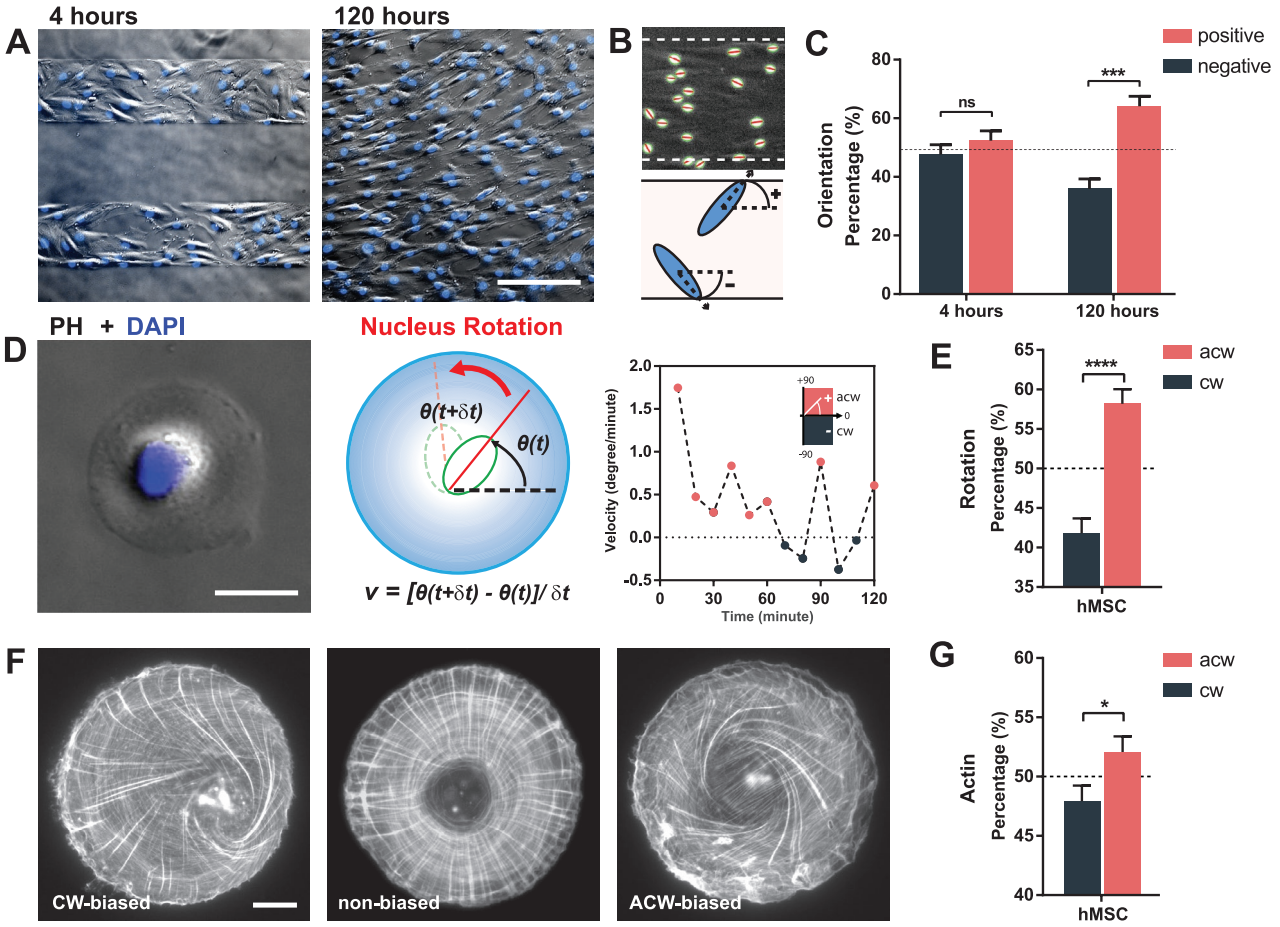

Figure 1. Chirality of hMSCs on micropatterns. A) Phase-contrast images (PH) with fluorescence-stained cell nucleus of hMSCs cultured on micropatterned stripes for 4 and 120 h. Scale bar: 200 µm. B) Processed cell nuclei on stripe pattern, with green lines showing the surrounding ellipses, red line showing the long axis of nucleus, and white dashed lines showing the horizontally aligned stripe boundary, where the definition of positive and negative orientation is based on the acute angle between nucleus direction and the stripe boundary. C) Percentage of positive/negative orientation at 4 h (n = 5 rows of stripes) and 120 h (n = 5 rows of stripes). D) Micropatterned single cell with fluorescence-stained cell nucleus (DAPI), through which the angular velocity of cell nucleus was calculated based on two consecutive snapshots in a time-lapse microscopy (10 min interval for total 2 h and 10 min). Scale bar: 40 µm. E) Percentage of CW or ACW nucleus rotation of each hMSC on gear patterns (n = 119 cells). F) Representative image of actin filament forming CW-biased (ACW 42.69%), non-biased (ACW 48.04%), and ACW-biased (ACW 60.95%) swirling pattern. Scale bar: 20 µm. G) Percentage of actin filament with CW/ACW bias within each hMSC on gear patterns (n = 38 cells).

change appeared at very early stage (3–5 days) prior to the maturation of other standard differentiation markers, suggesting an early commitment of cell chirality during differentiation.

We next explored the chirality during the lineage-specific differentiation at single cell level. The changed chiral orientation may involve other factors such as cell morphology and migration. For example, cells with adipogenic induction may migrate slower or less elongate, which may affect the expression of chiral orientation. To rule out this possibility, cells were re-suspended from the stripes on days 3 and 5, and re-seeded on gear patterns to assess their rotational bias. The results showed that undifferentiated cells and cells with osteogenic induction exhibited an ACW-biased rotation (Figure 2E,F). In contrast, cells with adipogenic differentiation exhibited a strong CW-biased rotation, which was consistent with the negative chiral orientation on micropatterned stripes. Together, our results provided a direct evidence that early differentiated cell chirality occurred in single cells, ruling out other potential factors such as changes of cell migration or cell shape that may contribute to the difference of multicellular orientation. More importantly, for early differentiating hMSCs on days 3 and 5, the chiral swirling of actin cytoskeleton was consistently observed, i.e., ACW bias in single cells with osteogenic induction and CW bias in single cells with adipogenic induction (Figure 2G,H). Thus, the early differentiated chirality involves nucleus rotation and the reconfigured chiral swirling of actin filament as early as 3 days after induction, which showed a direct evidence of early committed cell chirality occurring in single cells, and such chirality can provide early guidance of LR morphogenesis (Figure 2C,D) precedent to the maturation of other terminal differentiation markers (Figure S2D, Supporting Information).

We next explored whether such early changed chirality is a particular phenomenon in cells cultured on micropatterned stripes, or a general phenomenon in cells cultured in other conditions. To test it, hMSCs were first incubated in petri dishes

© 2020 Wiley-VCH GmbH

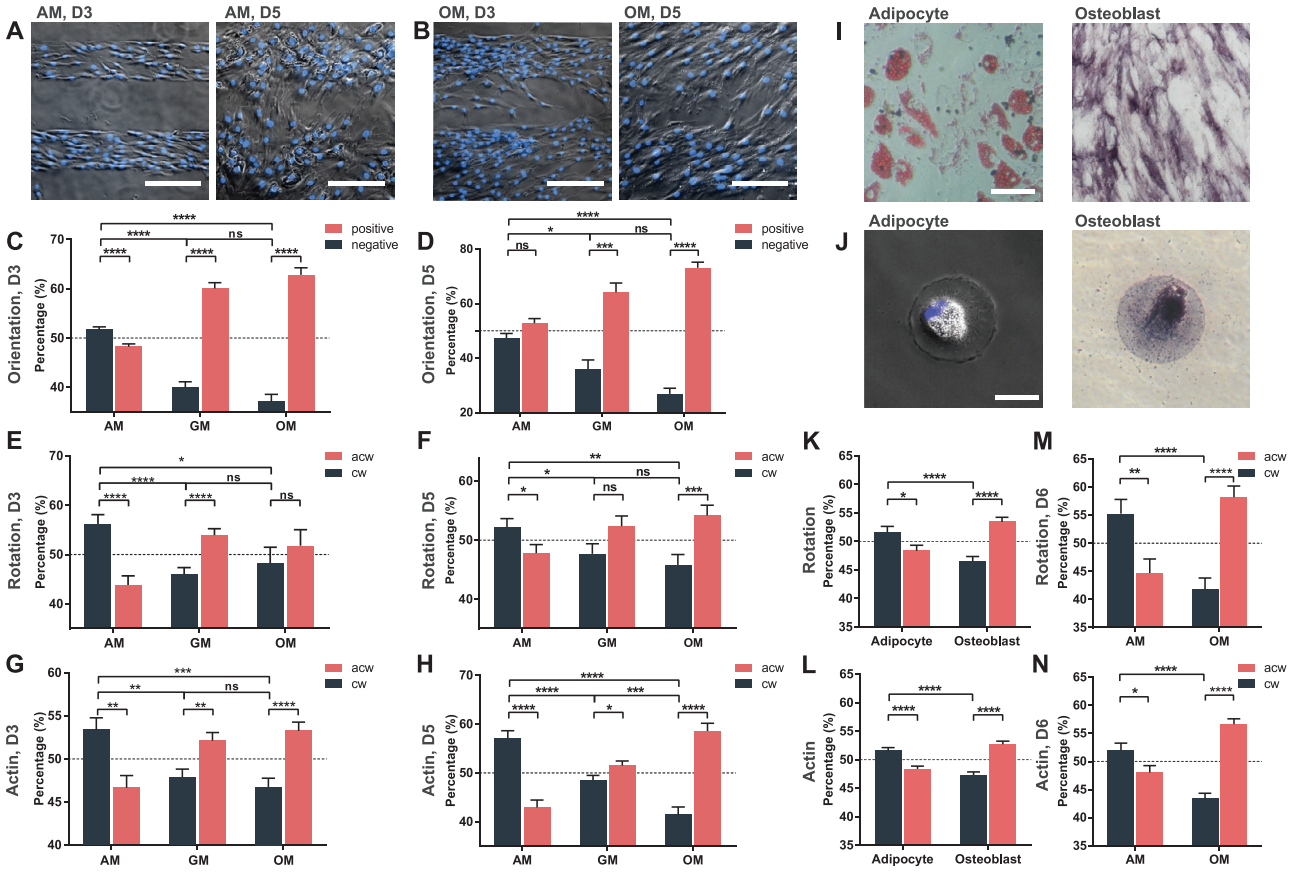

Figure 2. Evolvement of cell chirality during lineage-specific differentiation. A,B) PH images with fluorescence-stained cell nucleus of hMSCs on micropatterned stripe with A) adipogenic medium (AM) or B) osteogenic medium (OM) on day 3 (D3) and day 5 (D5). Scale bar: 200 μm. C,D) Percentage of positive/negative orientation on stripe on C) D3 and D) D5, where cell orientation in GM on D5 is redisplay from Figure 1C for comparison (n = 24, 25, 25, 6, 5, and 5 row of stripes). E,F) Percentage of CW/ACW nucleus rotation of each hMSC re-seeded from cells cultured on micropatterned stripes with GM, AM, or OM on E) D3 and F) D5 (n = 105, 129, 47, 66, 67, and 70 cells). G,H) Percentage of actin filament on gear patterns with CW/ACW bias within each hMSC re-seeded from cells cultured on micropatterned stripe with AM/GM/OM on G) D3 and H) D5 (n = 68, 99, 71, 28, 40, and 16 cells). I) Terminally differentiated adipocytes and osteoblasts after ≈3 weeks of induction, with adipocytes showing lipid stained by Oil Red O staining (red) and osteoblasts showing alkaline phosphatase (ALP) activity (purple). Scale bar: 100 μm. J) Single adipocyte and osteoblast on gear patterns for measurement of nucleus rotation, where lipid and ALP staining can still be positive after re-seeding. Scale bar: 40 μm. K) Percentage of CW/ACW nucleus rotation of each adipocyte and osteoblast on gear patterns (n = 348 and 492 cells). L) Percentage of actin filament with CW/ACW bias within each adipocyte and osteoblast on gear patterns (n = 139 and 187 cells). M) Percentage of CW/ACW nucleus rotation of each hMSC re-seeded from cells cultured in petri dishes with AM/OM on day 6 (D6) (n = 69 and 117 cells). N) Percentage of actin filament with CW/ACW bias within each hMSC re-seeded from cells cultured in petri dishes with AM/OM on D6 (n = 74 and 103 cells).

with AM or OM for 6 days (early stage of differentiation) or at least 18 days (terminally differentiated adipocytes and osteoblasts, as evidenced by Oil Red O and ALP activity, respectively, Figure 2I). Next, the differentiated cells were re-suspended and re-seeded onto gear patterns to measure the nucleus rotation (Figure 2J). We used nucleus rotation assay in this assessment because it avoids the ambiguity of other factors, e.g., cell migration and cell shape, and it needs lower number of cells, which is more practical because a significant amount of cells can be lost when re-suspending terminal differentiated osteoblasts/adipocytes. Of note, terminally differentiated cells can still exhibit differentiation marker after re-seeding on gear patterns (Figure 2J). Our results showed that the terminally induced adipocytes exhibited a CW-biased rotation, while the terminally induced osteoblast showed an ACW-biased rotation (Figure 2K). Such chiral bias is consistent with that of actin swirling in terminally differentiated osteoblasts and adipocytes (Figure 2L). More interestingly, cells induced for 6 days in regular petri dish exhibited similarly chirality as that of terminally induced cells, as viewed by the chiral rotation and swirling pattern of actin cytoskeleton (Figure 2M,N). Taking together, those results (nucleus rotation and actin swirling) are consistent with the results of nucleus rotation after 3 days of induction on stripe, indicating that the cells can commit to specific, lineage-dependent chirality at early stage of differentiation (3 days on stripe or 6 days on dish) and consistently express it at terminal stage.

The lineage-dependent cell chirality suggests that undifferentiated hMSCs may exhibit varied chirality from one batch to another, as different batches of hMSCs from different donors can show up to 218-fold differences in mRNA levels of ALP,[47] resulting in varied lineage commitment and differentiation

© 2020 Wiley-VCH GmbH

potential.[48] Here, we also observed donor-to-donor variances in the chirality of undifferentiated hMSC. Using one batch of hMSCs from a second donor (donor 2), we found an unbiased nucleus rotation on gear patterns (Figure S3A, Supporting Information). Also, for cells on micropatterned stripes for 3 days, we observed a negatively biased cell orientation (Figure S3B, Supporting Information) and CW-biased nucleus rotation after resuspension and re-seeding on circular micropatterns (Figure S3C, Supporting Information). To study the difference between these two batches, we evaluated the expression of adipogenic and osteogenic markers. We found that a significantly higher ratio of (adiponectin)/(ALP) of undifferentiated donor 2 cells, which suggested an increased adipogenic commitment of this donor 2 cells before induction (Figure S3D, Supporting Information) and explained the CW-biased rotation and negative cell orientation of this donor 2 cells (Figure S3A–C, Supporting Information). On the other hand, with adipogenic induction on stripes, this donor 2 cells still exhibited a negative cell orientation and CW-biased nucleus rotation; whereas they expressed positive orientation and ACW-biased nucleus rotation with osteogenic induction on stripes (Figure S3B,C, Supporting Information), which is consistent with that of donor 1 cells (Figure 2). Thus, while the donor-to-donor variance exists in chirality of undifferentiated hMSCs, the correlation between lineage-specific induction and cell chirality remains valid.

2.3. Treatment of Actin Inhibitors Regulating the Cell Chirality

Clearly, the early differentiated cell chirality is associated with the chiral swirling pattern of actin cytoskeleton. To further investigate the role of actin in cell chirality, we conducted actin inhibition on cells. We selected LatA, which inhibits actin polymerization by sequestering monomeric actin,[49] lysophosphatidic acid (LPA), which stimulates RhoA and the formation of actin filaments,[50] and CD, which prevents actin polymerization by its high affinity to growing ends of actin nuclei.[51] Undifferentiated hMSCs were seeded onto petri dish and incubated with GM, supplemented with LatA, LPA, and CD for 24 h. Subsequently, nucleus rotation assay was conducted by re-suspending and re-seeding those cells onto gear patterns, followed by fixation and actin staining. We found that dorsal stress fibers and transverse arc were retained in cells with LatA and LPA treatment, while the actin filaments were heavily disrupted in CD-treated cells (**Figure 3**A). Interestingly, LatA led to a distinct CW-biased swirling pattern of actin and nucleus rotation, which is consistent with a recent report[52] (Figure 3B,C). Notably, while the actin filament was not analyzable for cells with CD treatment (data not shown), CW-biased nucleus rotation was still observed, which is expected since CD and LatA have similar effect of inhibiting actin polymerization. In contrast, LPA treatment led to a neutral, non-biased actin pattern and nucleus rotation

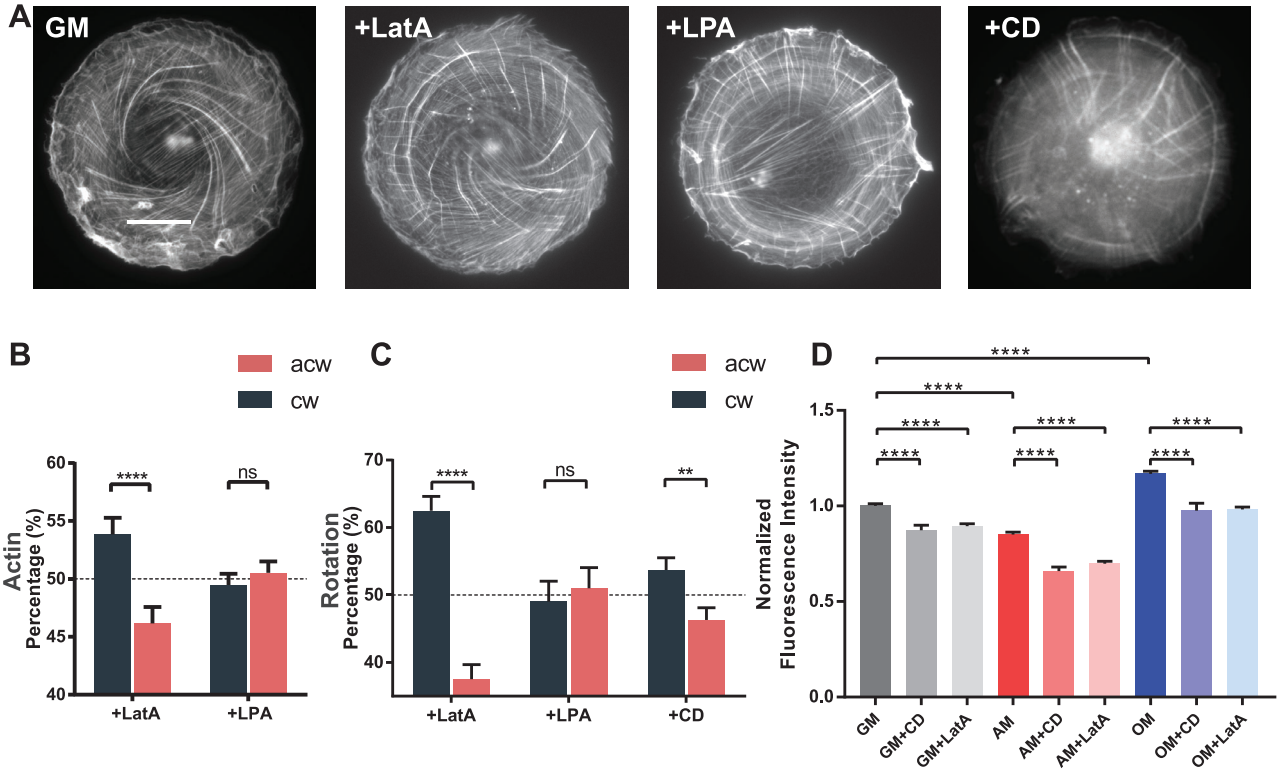

Figure 3. Treatment of actin inhibitors latrunculin A (LatA), lysophosphatidic acid (LPA), and cytochalasin D (CD) regulating the chirality. A) Representative fluorescence images of actin cytoskeleton in GM, GM+LatA, GM+LPA, or GM+CD. Scale bar: 20 µm. B) Percentage of actin filament with CW/ACW bias within each hMSC with LatA or LPA (n = 20 and 21 cells). C) Percentage of CW/ACW nucleus rotation of each hMSC with LatA, LPA, or CD (n = 42, 66, and 60 cells). D) Flow cytometry showing relative mean fluorescence intensity (MFI) of actin of cells in GM/OM/AM with/without LatA or CD, normalized by the intensity of hMSCs in GM. The number of events n = 5967 (GM), 2989 (GM+LatA), 1176 (GM+CD), 4116 (AM), 2249 (AM+LatA), 924 (AM+CD), 5742 (OM), 2976 (OM+LatA), and 812 (OM + CD).

© 2020 Wiley-VCH GmbH

(Figure 3B,C). Together, the results demonstrated that LatA and CD treatment can induce a CW-biased chirality.

The CW-biased nucleus rotation and swirling pattern of actin might be a particular phenomenon that only occurs when cells are cultured as single cells on circular micropatterns. To validate the universality of such induced chirality, we directly analyzed the nucleus rotation of hMSCs in the petri dish supplemented with LatA. By labeling and tracking each cell nucleus, the angular velocity was calculated based on the transient velocity between two consecutive images at each 10 min interval (Figure S4, Supporting Information). By comparing percentages of ACW and CW rotation each cell within the observation duration (6 h), we again observed a CW-biased rotation in culture supplemented with LatA (Figure S4, Supporting Information). Clearly, the treatment of LatA can indeed force a CW-biased chirality in both single cells on circular pattern and multicellular culture in petri dishes.

Previous reports have suggested that adipogenesis induction may reduce the expression of F-actin[45] and contractility.[29] Because LatA and CD treatment can recapture the CW-biased chirality similar to adipogenic induction, they may also induce other similar change in actin cytoskeleton. To test it, we conducted flow cytometry to quantify the expression of F-actin. Undifferentiated hMSCs were cultured in petri dish with AM/OM with/without LatA or CD for 24 h. Our results showed that the adipogenic induction indeed reduced the F-actin expression, while the osteogenic process increased it (Figure 3D). Interestingly, the supplement of LatA or CD in either GM, AM, or OM all reduced the F-actin. Taking together, our results suggests that adipogenic induction can cause combinatory effect of on cytoskeleton, i.e., suppression of F-actin and CW-biased chirality, and LatA or CD treatment can best resemble such early-expressed cytoskeletal changes (Figure 3D).

2.4. Cell Chirality Regulating Cell Differentiation

We next investigated whether lineage commitment can be regulated by such early differentiated chiral actin cytoskeleton. Regulation of cell differentiation has been reported with a closed feedback loop associated with cell mechanics. Examples include substrate stiffness[32,33,36,53] and micropatterned geometry,[30,31,35,54] in which evolvement of cell mechanics such as cell contractility and morphology during differentiation can later consolidate the commitment of lineage specification, therefore forming a positive feedback loop to engage the cell fate. In our results, the early committed chirality, as seen by CW-biased actin filament and nucleus rotation, which may possibly serve as the mechanical precursor to maturate the lineage commitment. To test this possibility, we conducted lineage-specific induction with LatA and CD treatment, which forces a CW-biased chiral actin cytoskeleton resembling cytoskeletal features upon adipogenic induction (Figure 3). Stem cells were first seeded and induced by AM, OM, or mixed medium (MM, AM: OM = 1:1) with/without LatA. After 9 days, we used standard staining of Oil Red O to mark adipocyte ($Lipid^+$) (**Figure 4**A,B) and calculated the percentage of adipocyte with respect to the total number of cells.[26,35] In addition, osteoblasts were stained by ALP activity and quantified by the optical absorbance at 595 nm (ALP^+) (Figure 4B,C). We found a pronounced increased percentage of adipocytes in AM or MM supplemented with LatA (Figure 4D,E). In contrast, a decrease of ALP activity was observed in cells in osteogenic and mixed induction with LatA (Figure 4F,G). Such upregulation of adipogenesis and downregulation of osteogenesis by LatA treatment were validated by qPCR, which showed corresponding expression of adipogenic marker (adiponectin and PPARγ) and osteogenic marker (ALP) (Figure 4H,I). Consistently, similar upregulation of adipogenic commitment was also observed in cells in MM with CD treatment (Figure 4J,K). Taking together, the results showed that the forced CW-biased chiral actin upon LatA or CD treatment can indeed upregulate the commitment of adipogenic differentiation.

While LatA or CD treatment can best simulate the actin cytoskeleton upon adipogenic induction by their dual effect on cytoskeleton, i.e., suppression of F-actin and CW-biased chirality, it is difficult to dissociate and decouple these two effects. As the suppression of F-actin was already known effective to enhance adipogenic commitment,[39,40] it is unclear whether CW-biased chirality can upregulate adipogenic differentiation. To rule out the role of reduced F-actin, we applied Noco. Noco is known to inhibit microtubule polymerization by binding to tubulin dimers,[55] but can on the other hand enhance actin polymerization through functional linkage between these two cytoskeletal networks.[56,57] Similar to actin inhibitors, undifferentiated hMSCs were treated by Noco for 24 h, followed by measurement of nucleus rotation and actin staining on gear patterns (**Figure 5**A). Interestingly, Noco treatment induced a dosage-independent CW-biased swirling pattern of actin and nucleus rotation (Figure 5B,C). However, the expression of F-actin was not reduced but even slightly increased (Figure 5D), which is opposite to the treatment of LatA or CD and consistent with previous reports.[56,57] More strikingly, using standard staining of Oil Red O and ALP activity (Figure 3E,F), we again found an upregulation of adipogenic differentiation (Figure 5G), while ALP activity was not decreased in OM+Noco (Figure 5H). This upregulation is again observed in MM, suggesting an enhanced commitment of adipogenic lineage (Figure 5I). Altogether, the results suggest CW chirality can itself serve as a key mediator in a closed feedback loop to promote adipogenic differentiation.

3. Discussion

The mechanical behaviors of stem cells are essential for their growth, migration, and differentiation. In this work, we used micropatterning to investigate the relationship between the cell chirality and cell differentiation. Our results showed that the ACW-biased chiral nucleus rotation of hMSCs was reversed to CW-biased with adipogenic induction, providing a direct evidence showing that differentiation is playing a role for the phenotype dependence of cell chirality. Interestingly, the response of cell chirality in 3 days on stripes or 6 days in petri dishes is much earlier than the common induction process which takes ≈3 weeks to terminal differentiation.[58] More strikingly, by cross-comparing treatment of LatA, CD, and Noco, we found that the forced CW-biased chirality in undifferentiated hMSCs resembling the early differentiated chirality upon adipogenic

© 2020 Wiley-VCH GmbH

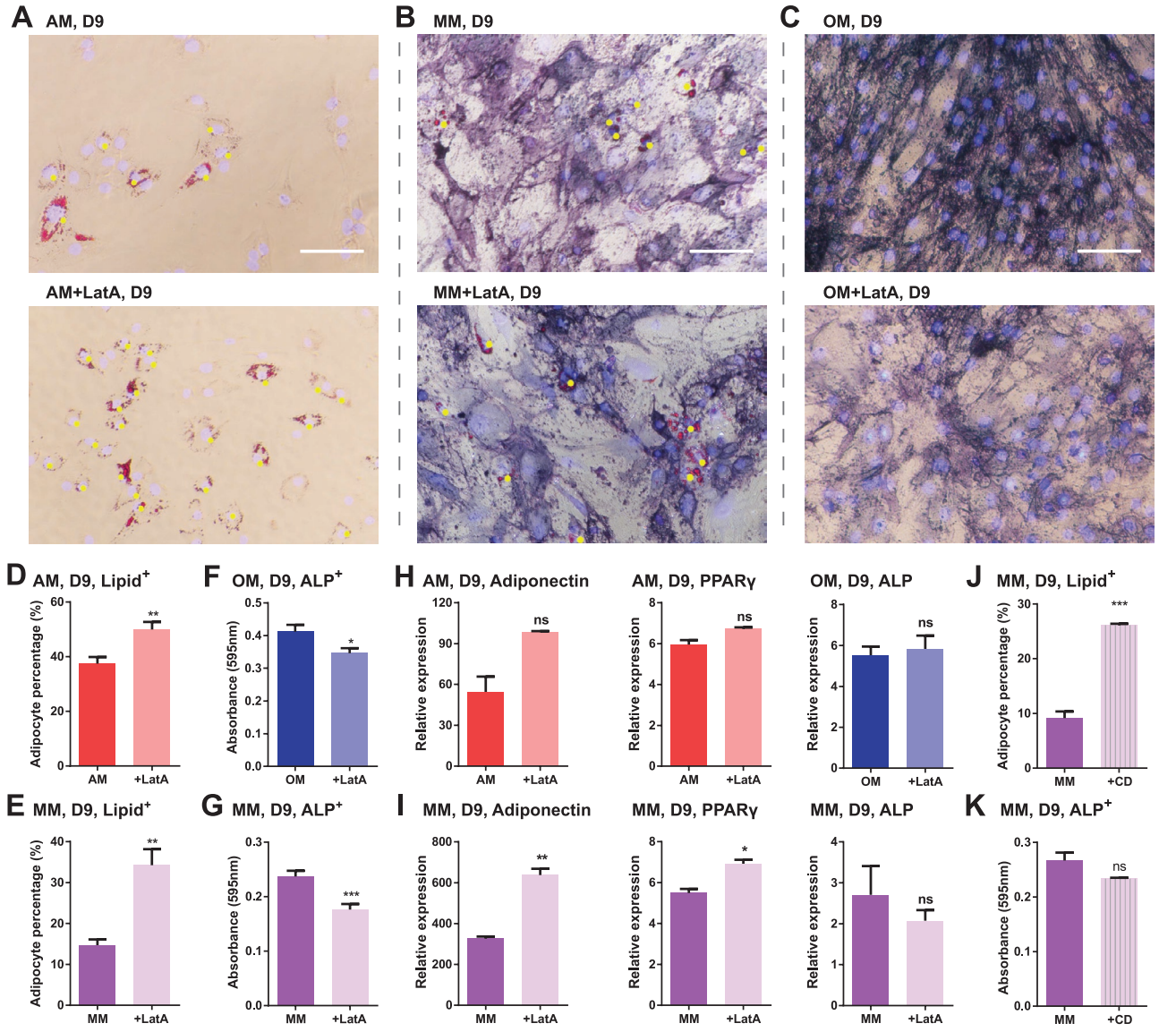

Figure 4. Adipogenic differentiation upregulated by LatA or CD treatment. A) Staining of Oil Red O of hMSCs in AM or AM+LatA for 9 days (D9), where the yellow dots mark cells stained lipids$^+$. B) Dual staining of Oil Red O and ALP activity of hMSCs in mixed medium (MM, AM:OM = 1:1) or MM+LatA for 9 days. C) Staining of ALP activity in OM or OM+LatA for 9 days, where the purple color represents ALP$^+$ cells. Scale bar: 200 μm. D,E) Percentage of lipids$^+$ cells in D) AM and E) MM with/without LatA (n = 6 and 3 wells). F,G) Optical absorbance of ALP$^+$ cells in F) OM and G) MM with/without LatA (n = 15 and 15 points). H) Relative expression of adipogenic markers (adiponectin and PPARγ) and osteogenic marker (ALP) in AM or OM (n = 2, 2, and 4 wells) with/without LatA. I) Relative expression of adipogenic markers (adiponectin and PPARγ) and osteogenic marker (ALP) in MM with/without LatA (n = 3, 3, and 3 wells). J) Percentage of lipids$^+$ cells in MM with/without CD (n = 3 and 3 wells). K) Optical absorbance of ALP$^+$ cells in MM with/without CD (n = 15 and 15 points).

induction can upregulate lineage commitment toward adipogenic differentiation. It suggests that, for the first time, the actin and the corresponding chirality may serve as the mechanical prerequisite before the completion of cell differentiation, providing new insights for such chiral-mechanics-related stem cell research.

Our findings of early differentiated chirality imply a possible requirement of early established LR morphogenesis for tissue/organ development. Cell chirality has been reported with a role to guide the LR asymmetry in tissue/organ morphogenesis.[1–4] Studies on early embryonic development suggested that blastomeres at eight-cell stage exhibit handed collective movement and uneven distribution of cells for subsequent LR fate inductions.[7] If such LR induction was not appropriately set, it may lead to incident of mirror imaging of unilateral defects and asymmetric trait in monozygotic twins.[59] Our previous studies on vascular mesenchymal cells showed that cell chirality can guide cell migration with rightward bias, which subsequently leads to self-organized LR asymmetry in collective cell orientation[60] and alignment of multicellular micro-tissue.[15,61] Here, using the collective cell orientation on micropatterned stripes as a simplified model of self-organized morphogenesis,[15] our

© 2020 Wiley-VCH GmbH

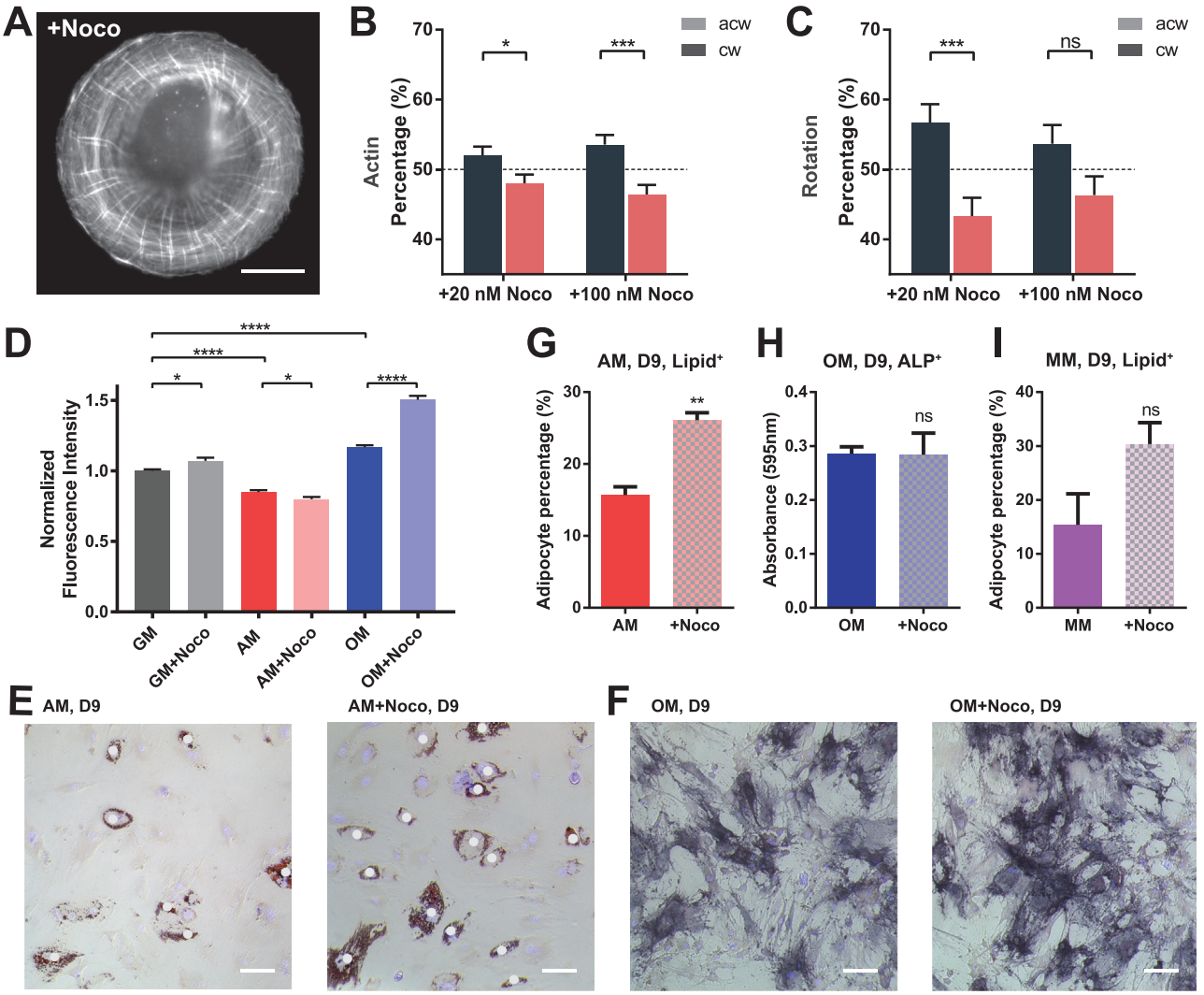

Figure 5. Adipogenic differentiation upregulated by nocodazole (Noco) triggered CW chirality. A) Representative fluorescence images of actin cytoskeleton in GM+Noco. B) Percentage of actin filament with CW/ACW bias within each hMSC with Noco ($n = 40$ and 45 cells). C) Percentage of CW/ACW nucleus rotation of each hMSC with Noco ($n = 38$ and 43 cells). D) Flow cytometry showing relative mean fluorescence intensity (MFI) of actin of cells in GM/OM/AM with/without Noco, normalized by the intensity of hMSCs in GM. The number of events $n = 1244$ (GM+Noco), 1544 (AM+Noco), and 1801 (OM+Noco). The data of GM, AM, and OM are redisplayed from Figure 3D for comparison. E) Staining of Oil Red O of hMSCs in AM or AM+Noco on D9. Scale bar: 200 µm. F) Staining of ALP activity in OM or OM+Noco on D9, where the purple color represents ALP$^+$ cells. Scale bar: 200 µm. G) Percentage of lipids$^+$ cells in AM with/without Noco ($n = 3$ and 3 wells). H) Optical absorbance of ALP$^+$ cells in OM with/without Noco ($n = 15$ and 15 points). I) Percentage of lipids$^+$ cells in MM with/without Noco ($n = 3$ and 3 wells).

results showed a direct evidence that early committed cell chirality occurring in single cells, including nucleus rotation and the reconfigured chiral swirling of actin filament, can provide early guidance of LR morphogenesis precedent to the maturation of other terminal differentiation markers. It suggests possible necessity of early exhibition of chirality to engage the lineage commitment and determine the primitive LR axis for the LR morphogenesis.

While the CW bias of nuclear rotation and actin swirling were clearly observed in single cells with adipogenic induction, the chirality of cell orientation is not as apparent as that of cells with osteogenic induction (Figure 2C,D). Indeed, the cell chiral orientation is a complicated process influenced by various factors like cell-cell communication and spatial constraints. As F-actin is downregulated upon the adipogenic induction (Figure 3D), it may also reduce the cell aspect ratio.[62] As a result, the CW bias accompanying with reduced F-actin and cell aspect ratio would lead to an ineffective intercellular alignment which prohibits the propagation and amplification of chiral orientation,[63] making the chirality of cell orientation with adipogenic induction not as distinctive as the CW bias of nuclear rotation and actin swirling of single cells.

The molecular mechanism underlying the reversed CW chirality remains unclear. It has been reported that the ACW chiral swirling pattern may arise from a possible axial rotation of dorsal stress fibers during its polymerization.[21] Similarly, RT-DIC microscopy has revealed that filopodia of neuronal growth cones and protrusions along the radial axis of

© 2020 Wiley-VCH GmbH

Dictyostelium cell exhibit a right-screw rotation, which later causes a right-handed cell migration on a 2D substrate.[20] With such conversion from molecular handedness to cellular motility, the proposed axial rotation of dorsal stress fibers well explained the ACW chiral nucleus rotation and actin swirling in undifferentiated hMSCs and osteoblasts. On the other hand, for the reversed chirality from ACW to CW, Tee et al. proposed that over expression of α-actinin-1 may cross-link the actin filament[64,65] and prohibit the filament rotation. As such, after accumulation of torsional stress within the filament, the radial filament may exhibit a screw-step rotating in a reversed direction, causing a CW-biased chirality.[3,21] We have tested the gene expression of α-actinin at the transcriptional level in such early committed CW chirality. However, in the qPCR results of hMSCs on stripes for 3 days, the α-actinin-1 expression was increased in ACW-biased cells with osteogenic induction, and a decreased expression was observed in CW-biased cells with adipogenic induction (Figure S5, Supporting Information). This observation, however, may be due to the overall suppression of F-actin after adipogenic induction (Figure 3D). Thus, the balance between F-actin and α-actinin-1 could be more crucial. Alternatively, the treatment of LatA was also reported able to induce CW chiral actin swirling of keratinocytes, and formin family protein DIAPH1 is required during the process.[52] Such finding is consistent with the CW chirality of adipocytes or hMSCs with LatA/CD/Noco treatment. Together, the CW chirality seems to require either suppression of actin polymerization or cross-linking of actin filament. Further investigation is needed to elucidate the mechanistic insights underlying the CW chirality.

4. Conclusion

In summary, using hMSCs on micropatterned ECM material, our results showed that hMSCs with adipogenic/osteogenic induction exhibit an early differentiated, opposite chiral bias, providing a direct evidence of lineage dependence of cell chirality. More importantly, using cross-comparison of treatment of LatA, CD, that forces a CW-biased nucleus rotation and actin swirling resembling the chirality upon adipogenic induction, we found an upregulated adipogenic commitment. Thus, our results suggest that the early differentiated CW chirality may serve as a key, mechanical mediator in a feedback mechanism to engage the adipogenic lineage as well as to coordinate the early establishment of LR morphogenesis during differentiation, providing a new insight in stem cell research, morphogenesis, and mechanobiology.

5. Experimental Section

Micropatterning: The micropatterning was achieved by photolithography. Glass substrate was first cleaned by a piranha solution (H_2SO_4:H_2O_2 (30%) = 3:1, Sigma-Aldrich) at 110 °C for 20 min and coated with hexamethyldisilazane (HMDS, Sigma-Aldrich) for 5 min. AZ5214 photoresist (PR, AZ Electronic Materials) was then spin-coated onto the HMDS surface at 3000 rpm for 30 s and baked at 95 °C for 2 min. UV exposure (MA6, Karl Suss) on desired geometric pattern, circular or gear patterns with area of 2827 μm^2 (radius = 30 μm), 5024 μm^2 (radius = 40 μm), and 7854 μm^2 (radius = 50 μm) or long stripes with width of 200 μm and length of 9000 μm, was used. After development (AZ400K, 1:2 dilution with deionized (DI) water, AZ Electronic Materials), the exposed substrate was dried under compressed air, treated by air plasma (Harrick Plasma) for 2 min (800 mTorr, 30 W) and followed by HMDS coating for another 5 min. Before cell seeding, the chip was incubated in fibronectin solution (FN, Life Technologies) at 25 μg mL^{-1} (in DI water) or laminin (Thermo Fisher) solution at 25 μg mL^{-1} (in DPBS) for 1 h and washing steps were conducted to remove remaining AZ5214 PR by 99% ethanol with 5 min for three times. Next, the chip was incubated in 1–2% Pluronic F127 (Sigma-Aldrich) in DI water for 50 min to coat the exposed HMDS region and prevent undesired cell adhesion. After that, these chips were ready for cell seeding and patterning.

Fabrication of PDMS Stencil Mask for Nucleus Rotation on Plasma-Treated Surface: First, SU-8 2050 (Microchem) was coated (1000 rpm for 40 s) and pre-baked (65 °C for 10 min and 95 °C for 90 min) onto a silicon wafer. UV exposure, post-bake (65 °C for 10 min and 95 °C for 30 min), and development (PEGMA) were followed to obtain the desired circular micro-pillar array. Next, the PDMS precursor consisting of three parts of SYLGARD 184 (ratio at 10:1) and two parts of SYLGARD 527 (ratio at 1:1) (both from Dow Corning) was dropped on the side of the micro-pillar array such that the gap between micro-pillars can be filled by capillary effect. Finally, the PDMS was solidified at a 70 °C hotplate for 30 min. Subsequently, the cured PDMS stencil mask with through-hole was peeled off and reattached to a non-treated petri dish. Followed by air plasma treatment for 5 min (800 mTorr, 30 W), the PDMS stencil mask was peeled off, and the dish was ready for cell seeding and patterning.

hMSC Culture and Differentiation: hMSCs (Lonza) were cultured in GM containing low-glucose Dulbecco's modified Eagle's medium (Life Technologies) mixed with 10% fetal bovine serum and 1% penicillin/streptomycin at 37 °C in a humid environment with 5% CO_2 and 95% air. Early passages (passages 4–8) of hMSCs were used in the experiment. Adipogenic and osteogenic differentiation were conducted following the supplier's instruction. For terminal adipogenic differentiation, adipogenic induction medium was used once the hMSCs were 100% confluence. Thereafter, the culture was supplied with three cycles of induction/maintenance medium (Lonza), i.e., adipogenic induction medium for 3 days followed by adipogenic maintenance medium for 3 days. After three cycles, the cells were kept in adipogenic maintenance medium for future use, during which the medium was replaced every 3 days. For terminal osteogenic differentiation, 3100 hMSCs cm^{-2} was plated in 24-well culture dish and refreshed with osteogenesis induction medium every 3 days for at least 18 days.

For induction of cells on micropatterned stripes, 25 000 cells cm^{-2} of hMSCs were pipetted onto the chip (0.7 cm × 0.9 cm) containing stripe patterns (width = 200 μm, length = 0.9 cm, total 17 stripes) for 60 min, followed by DPBS wash and cultured in hMSC GM for 2 additional hours. After that, patterned cells were refreshed with AM or OM. Control experiment was conducted by feeding patterned cells with hMSC GM.

For induction with LatA (Sigma-Aldrich), CD (Life Technologies), or Noco (Sigma-Aldrich), hMSCs were first cultured in 96-well plates with GM until 100% confluence. AM, OM, and MM (AM:OM = 1:1) were applied, supplemented with LatA at 50 × 10^{-9} M, CD at 200 × 10^{-9} M, or Noco at 20 × 10^{-9} M for 9 days, with medium changed every 3 days. An inhibitor-free induction was conducted for comparison. To be noted, in AM, adipogenic induction and maintenance medium were switched alternately following the supplier's instruction; while in MM condition, only adipogenic induction medium was applied.

Cell Orientation on Micropatterned Stripes: At 72 or 120 h, the nucleus of patterned hMSCs was stained with fluorescence by replacing the culture medium with staining medium at 1.0–2.0 μg mL^{-1} of bisBenzimide H 33342 trihydrochloride (Sigma-Aldrich) and incubated for 30 min. Next, after switching back to culture medium, images of phase-contrast microscopy and stained nucleus were captured by microscope (Nikon Ti-E). In detail, a series of images in both *x* (row) and *y* (column) directions was captured through "scan large image" function (Nikon Element). Afterward, a large image was stitched to cover patterned cells on stripes. For each imaged chip, every row of images was treated as

© 2020 Wiley-VCH GmbH

single sample for further statistical analysis and comparison. Image processing was implemented through MATLAB to conduct segmentation and orientation of each nucleus on stripes, as previously described[60] (MATLAB source code available at online repository: https://github.com/GiovannaHUANG/Outline-Etching-Cell-Chirality.git). Briefly, the raw images of fluorescence-stained nucleus were processed through Gaussian filter and thresholding to generate a binary image. However, after image binarization, some cell clusters in the binary image may be recognized as one bright region containing multiple cells, which makes the orientation analysis inaccurate. To segment individual nucleus from such clusters, an adaptive thresholding was further adopted to generate a secondary binary image with highlighted cell boundary. Then these two binary images were combined using Boolean addition operation to obtain enhanced concave regions to enhance the intersection among nucleus boundaries. By identifying cell cluster through comparing the area difference between the bright region and its surrounding minimum convex hull, the outside layer of cluster was iteratively eliminated until the cluster was segmented into single cells. Next, the orientation of each nucleus was surrounded by an ellipse, and the orientation was labeled based on the orientation of its long axis. As such, the cell orientation was defined as the acute angle with respect to the stripe boundary in either positive or negative value (Figure 1B). Thus, the percentages of positively and negatively aligned cells within one row were determined, and the significant difference between these two percentages was evaluated based on Student's *t*-test.

Measurement of Angular Velocity of Nucleus Rotation: Undifferentiated hMSCs, early-induced hMSCs, and terminally induced adipocyte/osteoblast were adopted for measurement. For cells with actin inhibitors, hMSCs were cultured in petri dish for 2 days and then treated with 50×10^{-9} M of LatA (Sigma-Aldrich), 10×10^{-6} M of LPA (Sigma-Aldrich), 200×10^{-9} M of CD (Life Technologies), or 20×10^{-9} or 100×10^{-9} M of Noco (Sigma-Aldrich) for 24 h, respectively. Before measurement, 2000 suspended cells were passaged and pipetted onto a chip containing around 3000 circular patterns or gear patterns of FN or laminin. After 60 min, the non-attached cells were flushed away with DPBS twice and attached cells were refreshed with culture medium or medium with inhibitors of the concentration above. For cells on plasma-treatment surface, cells were incubated for 3 days. Next, the nucleus was stained with fluorescence by replacing the culture medium with staining medium at 1.0–2.0 μg mL^{-1} of bisBenzimide H 33342 trihydrochloride (Sigma-Aldrich) and incubated for 30 min.

To measure the nucleus rotation, live cell incubator was used on microscope stage (Chamlide TC incubator system, Live Cell Instrument) with 100% humidity and 5% CO_2 in 37 °C to capture the images of stained nucleus in a series (10 min interval, total 2 h and 10 min). Next, the orientation of each nucleus was surrounded by an ellipse, and its long axis, which represents long axis of individual nucleus, was measured with respect to the horizontal reference to determine the angular alignment at each time point (Figure 1D). Next, the transient angular velocity of nucleus rotation was calculated based on the change of orientation angle ($\delta\theta = \theta_{t+1} - \theta_t$) divided by time interval (δt) between the two consecutive images. The ACW rotation was defined as positive (+), while the CW rotation was defined as negative (–) (Figure 1D). Afterward, the percentages of ACW or CW rotation of each cell in the duration were averaged among many cells. Thus, the significant difference between these two percentages was evaluated based on Student's *t*-test.

For cells rotation in petri dishes, hMSCs were first seeded at 5000 cells cm^{-2} density in GM with/without LatA supplement for 1 day. By labeling and tracking cell nucleus, the angular velocity was calculated based on the difference of cell long axis orientation, between two consecutive images at each 10 min interval (Figure S4, Supporting Information). The tracking process was conducted by linking cell in "prior frame image" with cell in "current frame image" when minor displacement was detected. For each traced cell, a continuous observation/measurement was carried out for 6 h, and the percentages of CW or ACW rotation of each cell was then calculated.

Adipogenesis and Osteogenesis Staining: For adipogenesis staining, the lipid droplet stained by Oil Red O was chosen as the differentiation marker. After the fixation with 4% paraformaldehyde (PFA) for 10 min and rinsing with DPBS, the cells were treated with 60% isopropanol (IPA, Sigma-Aldrich) for 5 min, stained with 3 mg mL^{-1} Oil Red O (Sigma-Aldrich) in IPA for 5 min, and then washed with DPBS. To calculate the percentage of adipocytes, cell with clear red lipid was counted. DAPI staining was further conducted to label cell nuclei, which allows counting of the total number of cells by image segmentation process as described in cell orientation measurement. Afterwards, the percentage of adipocyte was calculated.

For osteogenesis analysis, the staining of ALP activity was used. To perform it, cells were rinsed with 2×10^{-3} M Tris-HCL pH 9.5 buffer and then incubated in color reaction solution at 37 °C for 40 min. The color reaction solution was 200 μL NBT/BCIP stock solution (Roche) diluted in 10 mL detection buffer, which consisted of 0.1 M Tris-HCl pH 9.5, 0.1 M NaCl, and 0.05 M $MgCl_2$. After removing the color reaction solution and rinsing cell with 2×10^{-3} M Tris-HCL pH 9.5 buffer, cells were fixed with 4% PFA for 5 min. To quantify the stained ALP activity, measurement of optical absorbance was carried out based on the color appeared using a microplate reader (SpectraMax M5, Molecular Devices) at 595 nm wavelength, which was chosen based on the peak wavelength on absorbance spectrum. Alizarin red staining (Solarbio Life Sciences) was also used to label the osteogenic differentiation. Cells were fixed with 4% PFA for 10 min, rinsed by DPBS for three times, and incubated with the staining solution for 30 min at room temperature. After removing the staining solution, cells were washed with DPBS for five times, and finally DPBS was added to the well to avoid drying. Images were taken by microscope (Nikon, Ti-E).

Fluorescence Staining of Actin: For flow cytometry, cells were cultured in GM/AM/OM with/without 50×10^{-9} M of LatA (Sigma-Aldrich), 200×10^{-9} M of CD (Life Technologies), or 20×10^{-9} M of Noco (Sigma-Aldrich) for 24 h. Next, cells were trypsinized and centrifuged to form a pellet. The supernatant was removed, and cells were resuspended in 4% PFA on ice. After fixation for 20 min, cells were rinsed with DPBS with 0.1% Triton-X via centrifuge and resuspension. Next, signal enhancer (Invitrogen) was applied for 30 min, followed by fluorophore-conjugated phalloidin (1/40, Life Technologies) for 30 min on ice. Cells were rinsed and resuspended in DPBS with 0.1% Tween 20, and kept on ice before the measurement of relative intensity of F-actin by flow cytometer (BD FACSVerse, PE-Cy5.5). For cells cultured on circular or gear patterns for 3 h, they were first rinsed with DPBS and then fixed with 4% PFA for 10 min at 0 °C. After 0.1% Triton-X in DPBS for 5 min, signal enhancer (Invitrogen) was applied for 30 min, followed by fluorophore-conjugated phalloidin (1/40, Life Technologies) for 1 h. Washed with DPBS for three times and stained with DAPI (Sigma-Aldrich) for 5 min, sample was then washed by DPBS and mounted by Fluoromount-G (Thermo Fisher) for imaging. Cell actin was then imaged using a fluorescence microscope (Nikon Ti-E) through 40× oil lens.

Quantitative Analysis of Swirling Pattern of Actin Fibers: To quantitatively analyze the chirality of actin fibers, a square region containing the circular actin was cropped and applied adaptive threshold and Gaussian filter on each cropped image (Figure S6A, Supporting Information) to obtain a binary image with clear individual actin filaments (Figure S6B, Supporting Information). Focusing on the dorsal stress and transverse arcs, central region of binarized actin image (region diameter = 0.3 × image width) was removed. Based on the binary image, "bwmorph" function was applied in MATLAB to get filament skeleton (Figure S6C, Supporting Information), through which the outline pixels of a bright region were iteratively removed until all bright regions were downgraded to central, core lines. The core lines were further polished by removing the branches shorter than eight pixels. For remaining core lines longer than eight pixels and intersecting with other core lines, the intersecting joint were broken by removing the pixels at the intersection (Figure S6D, Supporting Information), allowing further simplification of actin filaments into single, unbranched core lines. To measure the orientation of core lines, each core line was surrounded by a minimum-size ellipse. For surrounding ellipses with aspect ratio >4, the core line was classified as straight lines (Figure S6E, Supporting Information). Otherwise, they were classified as curve lines (Figure S6F, Supporting Information). To quantitative analyze the swirling pattern of actin fibers, a polar coordinate with cell centroid

© 2020 Wiley-VCH GmbH

as the origin was first defined. For the straight line, the orientation was calculated based on the acute angle difference between the ellipse long axis and the tangential direction at the center of the surrounding ellipse. After that, each pixel of the enclosed core line was labeled with the orientation of the long axis of the surrounding ellipse (red line in Figure S6E, Supporting Information). For the curved line, a spline fitting from the core line was conducted (blue line in Figure S6F, Supporting Information). Next, at the location each pixel of the curved core line, the tangential line of the spline was determined, and its orientation was calculated same as the process above. Therefore, each pixel and its orientation mapping were created with one-on-one correspondence (Figure S6G, Supporting Information). Of note, the pixel orientation between –10° to 10° was excluded so the actin filaments aligning with the pattern boundary could be eliminated. Thus, a histogram of actin orientation with respect to the pixel number was summarized, where ACW and CW orientation was defined by orientation within 0° to 90° and –90° to 0°, respectively. Next, the percentage of actin with ACW or CW orientation was quantified based on the corresponding number of pixels (Figure S6H–J, Supporting Information). At last, to elucidate the rotational bias, percentage of actin with ACW and CW orientation from multiple, independent cells was analyzed. The percentage values were then averaged, and the significant difference between these two percentages was evaluated based on Student's *t*-test.

Quantitative PCR: Total RNAs were extracted using a commercial kit (PureLink RNA Mini Kit, Life Technologies), and its concentration was measured via BioDrop (BioDrop µLITE, UK). RNA solution from cell types was mixed with iScript cDNA synthesis kit (Bio-Rad) to convert it into cDNA. The procedure and thermal cycles were conducted following the manufacturer's instruction. After cDNA synthesis, 0.5 µg cDNA was added to SsoAdvanced universal SYBR Green Supermix from the commercial kit (SsoAdvanced Universal SYBR Green Supermix), together with the forward and reverse primers designed following the manufacturer's instruction. The primer used are for α-actinin-1,[66] adiponectin,[44] PPARγ[45] and ALP,[46] while the GAPDH primer would act as the endogenous normalizer (Table S1, Supporting Information). The sealed strips were loaded into the real-time PCR system in a thermal cycler over polymerase activation and DNA denaturation at 95 °C for 45 s. Under the 45 amplification cycles with denaturation at 95 °C for 15 s and annealing with extension at 60 °C for 1 min, a melt-curve was obtained. All samples were repeated four times. The qPCR results were analyzed by relative expression of in fold changes by ΔΔCt (cycle threshold method). The fold change, which reveals the difference in expression, was calculated based on the equation $2^{-\Delta\Delta Ct}$. In the equation, ΔΔCt means (ΔCt of experiment – [ΔCt of control]) and ΔCt represents the threshold cycle of target substrate by GAPDH.

Statistical Analysis: Prism (GraphPad Software) was used for statistical analysis and comparison. Analysis of statistical significance was carried out with two tailed Student's *t*-test between two groups. The numbers of samples (n) are specified in the figure legends for each comparison. Differences among groups were accepted as significant when $p < 0.05$ and the statistical significance was symbolized by ns ($p > 0.05$), * ($p < 0.05$), ** ($p < 0.01$), *** ($p < 0.001$), and **** ($p < 0.0001$). The error bar in figure is given as mean ± SEM unless specified otherwise.

Supporting Information

Supporting Information is available from the Wiley Online Library or from the author.

Acknowledgements

The authors are pleased to acknowledge the funding support from the Research Grant Council, University Grants Committee (no. N_CityU119/19, 11277516, and 11217217) and internal grants from City University of Hong Kong (6000632).

Conflict of Interest

The authors declare no conflict of interest.

Author Contributions

Y.Y.B. and S.Y.W. contributed equally to this work. T.-H.C. and R.H.W.L. conceived the study. Y.Y.B. and T.-H.C. designed the study and wrote the manuscript with input from all authors. Y.Y.B. and S.Y.W. performed most of the experiments. Y.Y.B. developed the image processing tool for the analysis of actin swirling. L.T.C. and H.K.K. performed the flow cytometry and qPCR analysis. H.H. and S.Y.W. performed the cell counting of adipocytes. Y.Z.H. and M.L.L. developed the image processing tool for the analysis of cell orientation.

Keywords

cell chirality, cytoskeleton, hMSCs, micropatterning, stem cell differentiation

Received: June 22, 2020
Revised: August 3, 2020
Published online:

[1] M. V. Danilchik, E. E. Brown, K. Riegert, *Development* **2006**, *133*, 4517.
[2] M. Lobikin, G. Wang, J. S. Xu, Y. W. Hsieh, C. F. Chuang, J. M. Lemire, M. Levin, *Proc. Natl. Acad. Sci. USA* **2012**, *109*, 12586.
[3] A. S. Chin, K. E. Worley, P. Ray, G. Kaur, J. Fan, L. Q. Wan, *Proc. Natl. Acad. Sci. USA* **2018**, *115*, 12188.
[4] P. Ray, A. S. Chin, K. E. Worley, J. Fan, G. Kaur, M. Wu, L. Q. Wan, *Proc. Natl. Acad. Sci. USA* **2018**, *115*, E11568.
[5] H. Yamanaka, S. Kondo, *Genes Cells* **2015**, *20*, 29.
[6] S. R. Naganathan, S. Furthauer, M. Nishikawa, F. Julicher, S. W. Grill, *elife* **2014**, *3*, e04165.
[7] C. Pohl, Z. R. Bao, *Dev. Cell* **2010**, *19*, 402.
[8] E. S. Noël, M. Verhoeven, A. K. Lagendijk, F. Tessadori, K. Smith, S. Choorapoikayil, J. den Hertog, J. Bakkers, *Nat. Commun.* **2013**, *4*, 2754.
[9] S. Hozumi, R. Maeda, K. Taniguchi, M. Kanai, S. Shirakabe, T. Sasamura, P. Spéder, S. Noselli, T. Aigaki, R. Murakami, K. Matsuno, *Nature* **2006**, *440*, 798.
[10] P. Spéder, G. Adám, S. Noselli, *Nature* **2006**, *440*, 803.
[11] K. Taniguchi, R. Maeda, T. Ando, T. Okumura, N. Nakazawa, R. Hatori, M. Nakamura, S. Hozumi, H. Fujiwara, K. Matsuno, *Science* **2011**, *333*, 339.
[12] K. Sato, T. Hiraiwa, E. Maekawa, A. Isomura, T. Shibata, E. Kuranaga, *Nat. Commun.* **2015**, *6*, 10074.
[13] W. Liu, Y. Bao, M. L. Lam, T. Xu, K. Xie, H. S. Man, E. Y. Chan, N. Zhu, R. H. W. Lam, T.-H. Chen, *ACS Nano* **2016**, *10*, 7409.
[14] J. S. Xu, A. Van Keymeulen, N. M. Wakida, P. Carlton, M. W. Berns, H. R. Bourne, *Proc. Natl. Acad. Sci. USA* **2007**, *104*, 9296.
[15] T.-H. Chen, J. J. Hsu, X. Zhao, C. Guo, M. N. Wong, Y. Huang, Z. Li, A. Garfinkel, C.-M. Ho, Y. Tintut, L. L. Demer, *Circ. Res.* **2012**, *110*, 551.
[16] X. Yao, J. Ding, *ACS Appl. Mater. Interfaces* **2020**, *12*, 27971.
[17] L. Q. Wan, K. Ronaldson, M. Park, G. Taylor, Y. Zhang, J. M. Gimble, G. Vunjak-Novakovic, *Proc. Natl. Acad. Sci. USA* **2011**, *108*, 12295.
[18] Y. W. Hu, X. Yao, Q. Liu, Y. Wang, R. L. Liu, S. Q. Cui, J. D. Ding, *Chin. J. Chem.* **2018**, *36*, 605.

© 2020 Wiley-VCH GmbH

[19] J. Fan, P. Ray, Y. W. Lu, G. Kaur, J. J. Schwarz, L. Q. Wan, *Sci. Adv.* **2018**, *4*, eaat2111.
[20] A. Tamada, M. Igarashi, *Nat. Commun.* **2017**, *8*, 2194.
[21] Y. H. Tee, T. Shemesh, V. Thiagarajan, R. F. Hariadi, K. L. Anderson, C. Page, N. Volkmann, D. Hanein, S. Sivaramakrishnan, M. M. Kozlov, A. D. Bershadsky, *Nat. Cell Biol.* **2015**, *17*, 445.
[22] G. L. Wang, M. L. Manning, J. D. Amack, *Dev. Biol.* **2012**, *370*, 52.
[23] J. Veerkamp, F. Rudolph, Z. Cseresnyes, F. Priller, C. Otten, M. Renz, L. Schaefer, S. Abdelilah-Seyfried, *Dev. Cell* **2013**, *24*, 660.
[24] K.-C. Hwang, J. Y. Kim, W. Chang, D.-S. Kim, S. Lim, S.-M. Kang, B.-W. Song, H.-Y. Ha, Y. J. Huh, I.-G. Choi, D.-Y. Hwang, H. Song, Y. Jang, N. Chung, S.-H. Kim, D.-W. Kim, *Proc. Natl. Acad. Sci. USA* **2008**, *105*, 7467.
[25] A. Shukla, J. H. Slater, J. C. Culver, M. E. Dickinson, J. L. West, *ACS Appl. Mater. Interfaces* **2016**, *8*, 21883.
[26] R. McBeath, D. M. Pirone, C. M. Nelson, K. Bhadriraju, C. S. Chen, *Dev. Cell* **2004**, *6*, 483.
[27] X. Yao, R. Peng, J. Ding, *Adv. Mater.* **2013**, *25*, 5257.
[28] M. D. Treiser, E. H. Yang, S. Gordonov, D. M. Cohen, I. P. Androulakis, J. Kohn, C. S. Chen, P. V. Moghe, *Proc. Natl. Acad. Sci. USA* **2010**, *107*, 610.
[29] J. P. Fu, Y. K. Wang, M. T. Yang, R. A. Desai, X. A. Yu, Z. J. Liu, C. S. Chen, *Nat. Methods* **2010**, *7*, 733.
[30] J. Lee, A. A. Abdeen, X. Tang, T. A. Saif, K. A. Kilian, *Biomaterials* **2015**, *69*, 174.
[31] L. Q. Wan, S. M. Kang, G. Eng, W. L. Grayson, X. L. Lu, B. Huo, J. Gimble, X. E. Guo, V. C. Mow, G. Vunjak-Novakovic, *Integr. Biol.* **2010**, *2*, 346.
[32] A. S. Mao, J.-W. Shin, D. J. Mooney, *Biomaterials* **2016**, *98*, 184.
[33] S. Even-Ram, V. Artym, K. M. Yamada, *Cell* **2006**, *126*, 645.
[34] K. Ye, L. P. Cao, S. Y. Li, L. Yu, J. D. Ding, *ACS Appl. Mater. Interfaces* **2016**, *8*, 21903.
[35] K. A. Kilian, B. Bugarija, B. T. Lahn, M. Mrksich, *Proc. Natl. Acad. Sci. USA* **2010**, *107*, 4872.
[36] A. J. Engler, S. Sen, H. L. Sweeney, D. E. Discher, *Cell* **2006**, *126*, 677.
[37] R. Peng, X. Yao, J. Ding, *Biomaterials* **2011**, *32*, 8048.
[38] X. Wang, S. Li, C. Yan, P. Liu, J. Ding, *Nano Lett.* **2015**, *15*, 1457.
[39] L. Chen, H. M. Hu, W. M. Qiu, K. K. Shi, M. Kassem, *Stem Cell Res.* **2018**, *29*, 76.
[40] P. Müller, A. Langenbach, A. Kaminski, J. Rychly, *PLoS One* **2013**, *8*, e71283.
[41] X. Yao, R. Peng, J. Ding, *Biomaterials* **2013**, *34*, 930.
[42] K. E. Worley, A. S. Chin, L. Q. Wan, *Stem Cells Int.* **2018**, *2018*, 1848605.
[43] S. Tojkander, G. Gateva, P. Lappalainen, *J. Cell Sci.* **2012**, *125*, 1855.
[44] M. Al-Nbaheen, R. vishnubalaji, D. Ali, A. Bouslimi, F. Al-Jassir, M. Megges, A. Prigione, J. Adjaye, M. Kassem, A. Aldahmash, *Stem Cell Res.* **2013**, *9*, 32.
[45] H. Sonowal, A. Kumar, J. Bhattacharyya, P. K. Gogoi, B. G. Jaganathan, *J. Biomed. Sci.* **2013**, *20*, 71.
[46] T. Eskildsen, H. Taipaleenmäki, J. Stenvang, B. M. Abdallah, N. Ditzel, A. Y. Nossent, M. Bak, S. Kauppinen, M. Kassem, *Proc. Natl. Acad. Sci. USA* **2011**, *108*, 6139.
[47] G. Friedl, H. Schmidt, I. Rehak, G. Kostner, K. Schauenstein, R. Windhager, *Osteoarthritis Cartilage* **2007**, *15*, 1293.
[48] T. R. J. Heathman, Q. A. Rafiq, A. K. C. Chan, K. Coopman, A. W. Nienow, B. Kara, C. J. Hewitt, *Biochem. Eng. J.* **2016**, *108*, 14.
[49] E. G. Yarmola, T. Somasundaram, T. A. Boring, I. Spector, M. R. Bubb, *J. Biol. Chem.* **2000**, *275*, 28120.
[50] Y. B. Sun, K. M. A. Yong, L. G. Villa-Diaz, X. L. Zhang, W. Q. Chen, R. Philson, S. N. Weng, H. X. Xu, P. H. Krebsbach, J. P. Fu, *Nat. Mater.* **2014**, *13*, 599.
[51] J. F. Casella, M. D. Flanagan, S. Lin, *Nature* **1981**, *293*, 302.
[52] S. Jalal, S. Shi, V. Acharya, R. Y.-J. Huang, V. Viasnoff, A. D. Bershadsky, Y. H. Tee, *J. Cell Sci.* **2019**, *132*, jcs220780.
[53] K. Ye, X. Wang, L. Cao, S. Li, Z. Li, L. Yu, J. Ding, *Nano Lett.* **2015**, *15*, 4720.
[54] R. Peng, X. Yao, B. Cao, J. Tang, J. Ding, *Biomaterials* **2012**, *33*, 6008.
[55] J. Hoebeke, G. V. Nijen, M. D. Brabander, *Biochem. Biophys. Res. Commun.* **1976**, *69*, 319.
[56] M. T. A. Muller, R. Schempp, A. Lutz, T. Felder, E. Felder, P. Miklavc, *Sci. Rep.* **2019**, *9*, 11973.
[57] K. M. Smurova, A. A. Birukova, A. D. Verin, I. B. Alieva, *Biol. Membr.* **2008**, *25*, 181.
[58] M. F. Pittenger, A. M. Mackay, S. C. Beck, R. K. Jaiswal, R. Douglas, J. D. Mosca, M. A. Moorman, D. W. Simonetti, S. Craig, D. R. Marshak, *Science* **1999**, *284*, 143.
[59] S. Aw, M. Levin, *Development* **2009**, *136*, 355.
[60] Y. Huang, Y. Bao, H. K. Kwong, T. H. Chen, M. L. Lam, *Biotechnol. Bioeng.* **2018**, *115*, 2595.
[61] T. H. Chen, X. L. Zhu, L. T. Pan, X. J. Zeng, A. Garfinkel, Y. Tintut, L. L. Demer, X. Zhao, C. M. Ho, *Biomaterials* **2012**, *33*, 9019.
[62] D. A. Young, Y. S. Choi, A. J. Engler, K. L. Christman, *Biomaterials* **2013**, *34*, 8581.
[63] H. K. Kwong, Y. Z. Huang, Y. Y. Bao, M. L. Lam, T. H. Chen, *ACS Biomater. Sci. Eng.* **2019**, *5*, 3944.
[64] K. Djinović-Carugo, P. Young, M. Gautel, M. Saraste, *Cell* **1999**, *98*, 537.
[65] P. Roca-Cusachs, A. del Rio, E. Puklin-Faucher, N. C. Gauthier, N. Biais, M. P. Sheetz, *Proc. Natl. Acad. Sci. USA* **2013**, *110*, E1361.
[66] E. Y. N. Lam, D. Beraldi, D. Tannahill, S. Balasubramanian, *Nat. Commun.* **2013**, *4*, 1796.

© 2020 Wiley-VCH GmbH